Electron Paramagnetic Resonance

Rico Schmidt and Guido Falk von Rudorff (Group M4)

I Introduction

Electron Paramagnetic Resonance (EPR) is a technique investigating samples by measuring transitions of unpaired electron spins in paramagnetic material. It has been applied to a broad range of samples like biological systems[1, 2], semiconductors[1] and transition materials[1, 3].

I.A Level Splitting

In general, any total spin $\mathbf{S}$ induces a magnetic moment $\boldsymbol{\mu}$ given by

$$\boldsymbol{\mu} = -\frac{g_e \mu_B}{\hbar}\mathbf{S} \tag{1}$$

where g_e is the material dependent g factor and μ_B the constant Bohr magneton[4]. Due to the linear dependency, paired spins do not contribute to any magnetic moment. The spin $|\mathbf{S}| = \sqrt{S(S+1)}\hbar$ is quantized; usually, its $\hat{\mathbf{e}}_z$ component is given as quantum number $m_s \in \{-s, -s+1, \ldots, s\}$[5].

For $S \neq 0$, there are different levels m_s which are subject to splitting due to the Zeeman effect.

$$E(m_s) = E_0 + g\mu_B B_0 m_s \tag{2}$$

where E_0 is the energy level without any external magnetic field $\mathbf{B} = B_0\hat{\mathbf{e}}_z$. Again, g denotes the g factor[5]. For induced transitions, the selection rule is $\Delta m_s = \pm 1$. For unpaired electrons, however, this selection rule is observed for all transitions, as $S = \frac{1}{2}$ and, hence, $m_s \in \{-\frac{1}{2}, \frac{1}{2}\}$.

The previous formulas are based on the assumption that the response of the material on the external magnetic field is isotropic. For some samples of this experiment, this is not the case. The most general form of keeping track of this anisotropy is extending the normal Hamiltonian

$$\hat{\mathbf{H}} = -g\mu_B \mathbf{B}\mathbf{S} \tag{3}$$

to include the tensor $\hat{\mathbf{g}}$ instead of the Landé g factor[1]. Hence, the Hamiltonian can be written as

$$\hat{\mathbf{H}} = -\mu_B \mathbf{B}\hat{\mathbf{g}}\mathbf{S} \tag{4}$$

Without loss of generality, the $\hat{\mathbf{g}}$ tensor can be diagonalized for all samples by representing the coefficient matrix in its pricipal axes basis[1]. Thence, the general form is given by

$$\hat{\mathbf{g}} = \begin{pmatrix} g_{xx} & 0 & 0 \\ 0 & g_{yy} & 0 \\ 0 & 0 & g_{zz} \end{pmatrix} \tag{5}$$

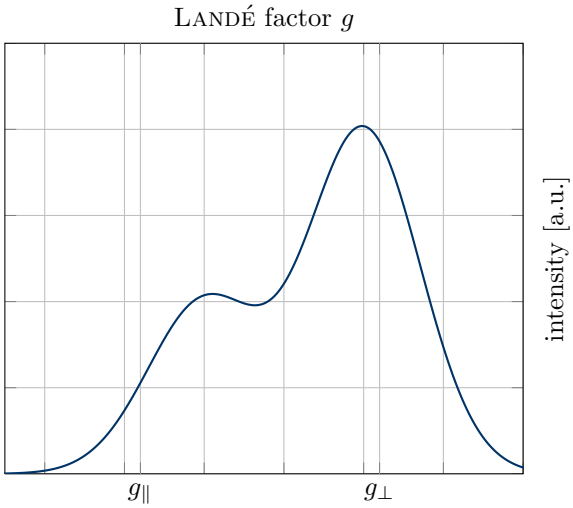

Figure 1. Schematic contributions of g values to the total signal when the axis of the external magnetic field does not match any of the pricipal axes[6] for $g_\perp > g_\parallel$. The shift between the highlighted g values and the peaks is a result from summing over all differential Gaussians.

Moreover, some materials allow for further simplification: at least one sample shows two g factors $g_\perp$ and $g_\parallel$ depending on the orientation of the external magnetic field with respect to the pricipal axes. In that case, we have[1]

$$g_\parallel = g_{zz} \qquad g_\perp = g_{xx} = g_{yy} \tag{6}$$

for an external magnetic field along $\hat{\mathbf{e}}_z$. In case of improper alignment, the relative contribution of is $g_\perp$ and $g_\parallel$ smeared as shown in Figure 1. In that case, the EPR peaks and, hence, their differential representation get asymmetric[6]. The angular dependency of the g factor is given by[6]

$$g(\varphi) = \sqrt{g_\parallel^2 \cos^2\varphi + g_\perp^2 \sin^2\varphi} \tag{7}$$

For single electrons in hydrogen-like atoms, the g factor is given[1, 5] as

$$g = \frac{3}{2} + \frac{s(s+1) - l(l+1)}{2j(j+1)} \tag{8}$$

For most radicals, g is very close to 2, only if very few cases g may be about twice as large[2].

For this experiment, one has to keep in mind two additional effects. The first of which is the nuclear Zeeman effect and the latter of which is the hyper fine interaction. The nuclear Zeeman interaction is similar to the one for the unpaired electrons and is given by

$$E(m_s, m_I) = E(m_s) + g_n \mu_N B_0 m_I \tag{9}$$

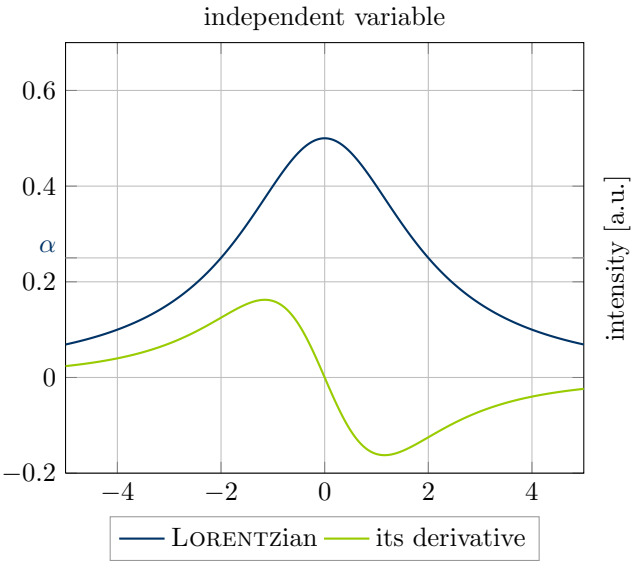

Figure 2. Lorentzian and its derivative for $a = 2$ and $x_0 = 0$ as example for the peak shape in the original and differential spectrum. α denotes the threshold for the FWHM.

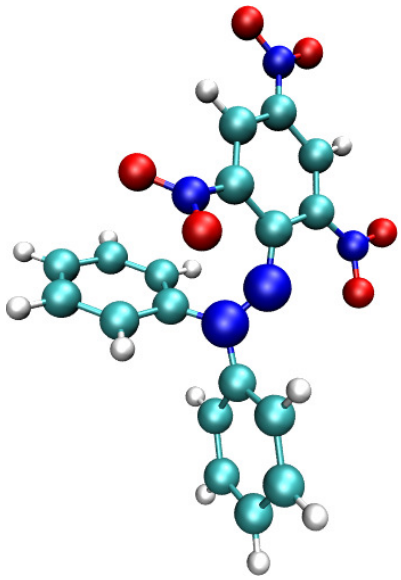

Figure 3. Conformation of DPPH. Rendered using data from[7]. The oversized nitrogen atoms are the location of the unpaired electron.

where m_I denotes the $\hat{\mathbf{e}}_z$ component of the nuclear spin and μ_N is the nuclear magneton. The g factor g_n can be different from the previous definitions, though[4, 5].

The hyperfine interaction is only visible if two conditions are met[9]: the nuclear spin I is non-zero and the electron is in an s-orbital[2]. Then, a small energy contribution has to be added for each of the n nuclear spins $\mathbf{I}_n$

$$\Delta E = \sum_n \mathbf{S}\hat{\mathbf{A}}\mathbf{I}_n \tag{10}$$

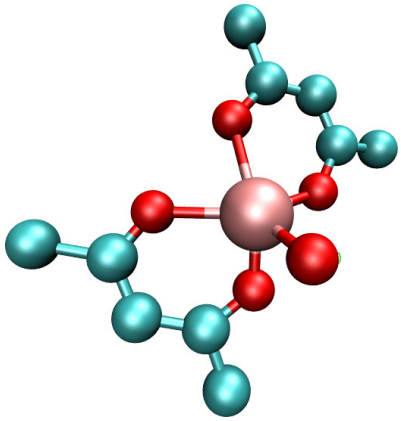

Figure 4. Conformation of vanadyl-acetylacetonate. Rendered using data from[8]. The oversized vanadium atom is the location of the unpaired electron.

where $\hat{\mathbf{A}}$ is an anisotropic tensor. The isotropic part of which can be factored out as a scalar[9], leaving only the anisotropic part as tensor.

The selection rule for these two additional effects is $\Delta m_I = 0$.

Based on this splitting, the main idea of EPR now is to induce transitions between splitted energy levels in order to measure the g factors of the hyperfine coupling constant A. As mentioned before, the external field $\mathbf{B_0}$ is necessary to induce the splitting. In order to probe the energy levels, a second field $\mathbf{B_1}$ is needed. In order to avoid any influence on the level splitting, it is experimentally advantageous to keep both magnetic fields perpendicular to each other. Transitions according to the selection rules can only be induced by the modulating external field $\mathbf{B_1}$ in case the occupation number for the corresponding energy levels is sufficiently different[4].

Given this setup, the g factor can be calculated[1] from the measured resonance frequency ω

$$g = \frac{h\omega}{\mu_B B_0} \tag{11}$$

In general, the peak shape in EPR spectra mostly follows[3, 10] the Lorentzian around x_0

$$I(x) = \frac{\kappa}{\pi} \frac{a}{(x - x_0)^2 + a^2} \tag{12}$$

with spin density κ. κ equals the integral of the Lorentz curve. In the following introductory part, we will assume $\kappa = \pi$. Although the shape resembles more a Gaussian if analyzed far from the maximum of the peak[6] at x_0, the shapes are well approximated by Lorentz curves. In general, the peak shape depends on the relaxation processes. The combination of both profiles seldom is required[1]. In order to tell nearby peaks apart, only the differential spectrum is analyzed in most cases. There, the Lorentzian follows

$$\frac{dI(x)}{dx} = -\frac{2a(x - x_0)}{((x - x_0)^2 + a^2)^2} \tag{13}$$

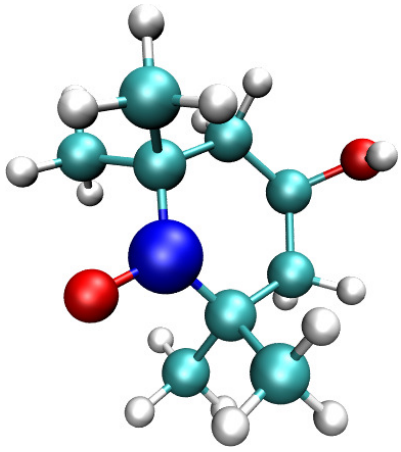

Figure 5. Conformation of 4 hydroxy tempo. Rendered using data from[12]. The oversized nitrogen atom is the location of the unpaired electron.

Table I. g factors for various materials.

material	g	sources
DPPH	(2.0036 ± 0.0003)	[1, 13]
vanadyl-acetylacetonate	(1.970 ± 0.001)	[9]
copper sulfate pentahydrate $\parallel$	(2.27 ± 0.01)	[9]
copper sulfate pentahydrate $\perp$	(2.08 ± 0.1)	[9]
4 hydroxy Tempo	(2.006 ± 0.001)	[9]
free electron	2.0023	[1]

Figure 2 shows both the peak positions and the full width at half maximum (FWHM) for both $I(x)$ and its derivative. The FWHM of the LORENTZian is $2a$ and the peak to peak difference of its derivative is $2a/\sqrt{3}$ for the x axis.

In solutions, the interaction of the spins is both frequent and strong[1]. Hence, the anisotropic part of the signal has a tendency to average out[1, 11]. This may lead to a smaller number of detectable hyperfine transitions[10]. The signal itself is slightly distorted by collision-induced relaxation[3].

In general, the signal from the sample has low intensity. Thus, the setup uses a lock-in amplifier which modulates the field B_1 with a high frequency ω_L

$$B_{\text{eff}} = B_1 + B_L \cos \omega_L t \tag{14}$$

This introduces two additional parameters to keep track of. The frequency defines a cutoff. For very high frequencies, the signal to noise ratio of the measured data is vanishing[3]. For very low frequencies, practically no noise can be filtered out. Hence, one has to select a value somewhere inbetween. Empirical values are about one tenth of the peak to peak linewidth of the LORENTZian, that is $0.2a$[3]. For overmodulated signal peaks, the enclosing function in the differential spectrum has to be taken as peak shape[6]. For the modulation amplitude B_L, one has to avoid saturation effects that blur the peak

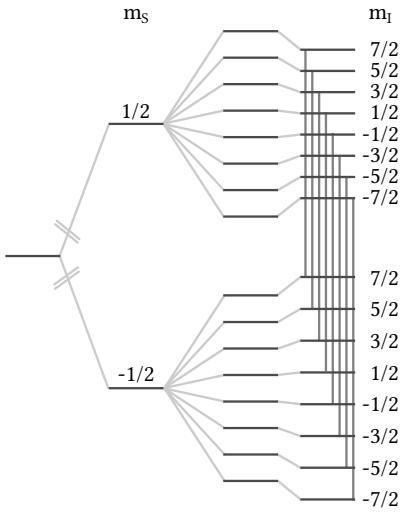

Figure 6. Energy level diagram for vanadyl (schematic, not to scale). The leftmost energy level is the degenerate one without any splitting. The second column arises from the electron ZEEMAN effect, the third column shows the nuclear ZEEMAN effect and the last one the shift due to the anisotropy. Hence, we have eight transitions, which are indicated by the vertical lines.

shape and hence make it more and more different from the LORENTZ peak[3]. Although this variation can be calculated, suggested values for B_L are a little bit smaller than a[3]. The saturation is a result of equilibration of the occupation numbers for the energy levels that are part of the transisitions. This saturation effect can be effective for low field strengths B_1 as well[6].

For crystals, the linewidth is affected by spin-lattice relaxation. In some cases, this relaxation process is the main cause for line broadening[6]. In general, the relaxation processes are similar to the ones for nuclear magnetic resonance (NMR)[11].

As the frequencies for ESR are much higher than the ones for NMR, one can not stick to an oscillating circuit as resonator[11]. Thence, we use a klystron together with a cavity for microwave generation.[9]

I.B Materials

Throughout this experiment, a broad range of materials is used. Table I lists their g factors; Figures 3, 4 and Figure 5 show their conformation. They are either polycrystalline powder, solutions or crystals. In general, the radical concentration can be upper bounded by $10^{13}\,\text{cm}^{-3}$[6]. Comparing peak integrals, one can compare relative radical concentrations[6]. This is even possible for the case of asymmetric peaks[1].

DPPH is used as crystalline powder. The radical nitrogen atom has a nuclear spin of 1. As there are two of them, we expect five symmetric fine structure components with relative intensities 1:2:3:2:1[6, 14–16]. This splitting may be too small to observe with this setup. DPPH is widely used in ESR as reference sample[1].

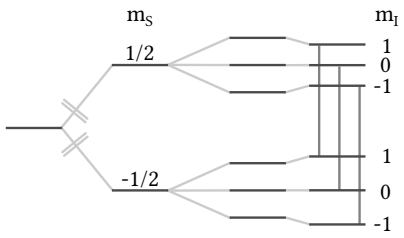

Figure 7. Energy level diagram for tempol (schematic, not to scale). The leftmost energy level is the degenerate one without any splitting. The second column arises from the electron Zeeman effect, the third column shows the nuclear Zeeman effect and the last one the shift due to the anisotropy. Hence, we have three transitions, which are indicated by the vertical lines.

The vanadium atom in vanadyl has nuclear spin of 7/2[4]. Hence, we expect eight peaks of identical intensity in the spectrum, as shown in Figure 6.

For tempol, the oxygen radical has spin 0. This only holds for ^{16}O, as the stable isotope ^{17}O has a spin of 5/2. The splitting we observe in the experiment is due to the nitrogen atom, which is expected to have a nuclear spin of 1. Hence, we expect three peaks in the spektrum, as shown in Figure 7.

I.C Quality Factor

The sensitivity of the spectrometer is given by the quality factor Q[9]

$$Q = \frac{f}{\Delta f} \tag{15}$$

where f is the central frequency of the spectrometer and Δf denotes the FWHM of the central frequency. Typically, the Q factor is between 2000 and 3000[3] and depends on the resonator used for the setup[10].

II Experiment

II.A Hilbert-Transformations

During the experiment, we measured a mixture of absorption and dispersion signal components. Although we tried to get pure absorption spectra, as described later on, we were not succesful in tuning the experiment to match the microwave phase requirement. The (differential) absorption spectra give more distinct results, as they show a zero crossing at the real peak position, whereas the the (differential) dispersion spectra show a maximum at the peak position. This section gives a overview over the method used in order to analyze the spectra during the rest of the protocol, so we will not need to come back to this description over and over again.

There are several options how to deal with mixed spectra[1]. The first one is based[17] on the idea of manual fitting of a combination of both absorption and dispersion

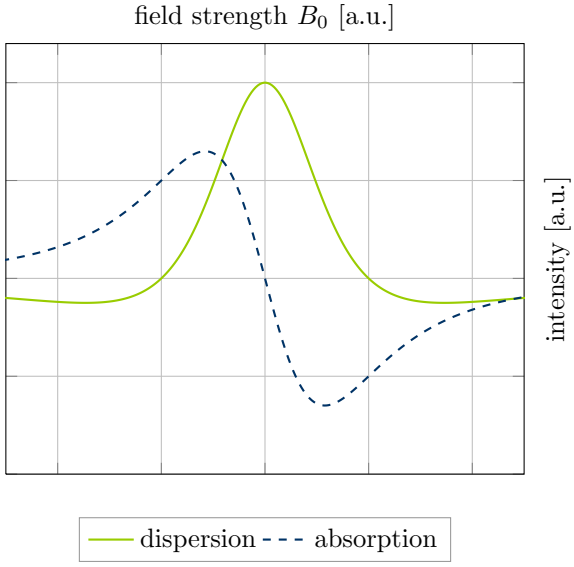

Figure 8. Differential Lorentzian for the dispersion and absorption mode[1].

spectra. Unfortunately, they do not add up linearly, so a rather tedious manual comparison of the measured spectra to several precomputed ones is the time-consuming part of this method. As the comparison has to be done manually, there is no easy and reliable way to perform this analysis in an automated way. Hence, we use the second way[1]: we use a Hilbert transformation, more specifically, the Kramers-Kronig relations[1]

$$\chi'(B) = \chi'(\infty) + \frac{2}{\pi}\int_0^\infty \frac{B'\chi''(B')}{B'^2 - B^2} dB' \tag{16}$$

$$\chi''(B) = -\frac{2B}{\pi}\int_0^\infty \frac{\chi'(B') - \chi'(\infty)}{B'^2 - B^2} dB' \tag{17}$$

These two equations relate the dispersion mode χ' and the absorption mode χ''. For a Lorentz peak, Figure 8 shows the differential spectra of the two modes.

Mathematically, applying the Hilbert transformation $\mathcal{H}$ to the measured data χ_M allows to invert the mixture components[1]. Comparing the transformation result χ_C to χ_M allows to determine the mixture of χ' and χ''. In order to do so, we define two properties of any given spectrum $\chi(B)$: $D(\chi)$ and $A(\chi)$. For each spectrum χ, there is a minimal and a maximal value. The higher absolute value of these two is called $D(\chi)$, the smaller absolute value will be referred to as $A(\chi)$. This way, the sign of the spectrum does not matter for the further analysis. The mixture φ of χ' (dispersion) and χ'' (absorption) then is given by[1]

$$\varphi = \left[\frac{2A(\chi'')}{A(\chi'') + D(\chi'')} - \frac{2A(\chi')}{A(\chi') + D(\chi')}\right] \cdot \left[1 - \frac{2A(\chi')}{A(\chi') + D(\chi')}\right]^{-1} \tag{18}$$

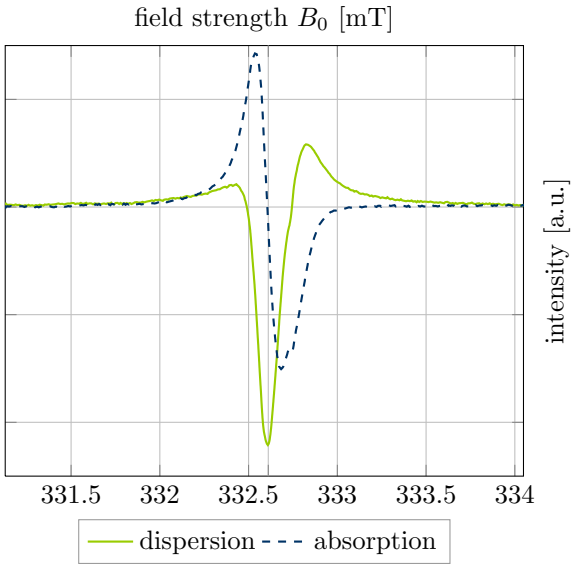

Figure 9. Sample result of the absorption-dispersion decomposition for DPPH. The peak position is the maximum of the dispersion curve and the zero crossing of the absorption curve. The peak position is at $(332.6084 \pm 0.0025)\,\mathrm{mT}$.

That way, we can represent χ_M as

$$\chi_M = \varphi\chi'' + (1-\varphi)\chi' \tag{19}$$

In general, the HILBERT transformation is linear

$$\begin{aligned}\mathcal{H}(\chi_M) &= \varphi\mathcal{H}(\chi'') + (1-\varphi)\mathcal{H}(\chi') && (20)\\ &= (1-\varphi)\chi'' - \varphi\chi' = \chi_C && (21)\end{aligned}$$

This is the only way to fulfill the inversion property of $\mathcal{H}$

$$\mathcal{H}(\mathcal{H}(\chi)) = -\chi \tag{22}$$

Equations (19) and (21) form a system of linear equations. There is exactly one solution

$$\chi' = \frac{-\varphi\chi_C + (1-\varphi)\chi_M}{(1-\varphi)^2 + \varphi^2} \tag{23}$$

$$\chi'' = \frac{(1-\varphi)\chi_C + \varphi\chi_M}{(1-\varphi)^2 + \varphi^2} \tag{24}$$

In the following, we will transform any spectrum χ_M into the corresponding absorption spectrum χ''. In order to illustrate the reliability of both the method and the *python* program calculating the transformations using *scipy*, Figure 9 contains both χ' and χ'' calculated from a sample spectrum χ_M recorded during the adjustment procedure.

The calculations carried out above assume the recorded spectrum to be dominated by absorption[1]. If this is not the case, φ is outside of $[0, 1]$. Thence, we swap the roles of χ_M and χ_C in order to keep the relations. This may mess up the sign conventions. As exchanging the sign is the same as shifting the phase of the lock-in amplifier by π, the physical content of the measurement remains unchanged. The following diagrams are not kept in sync with the sign convention, as they rather should reflect the measured data as far as possible.

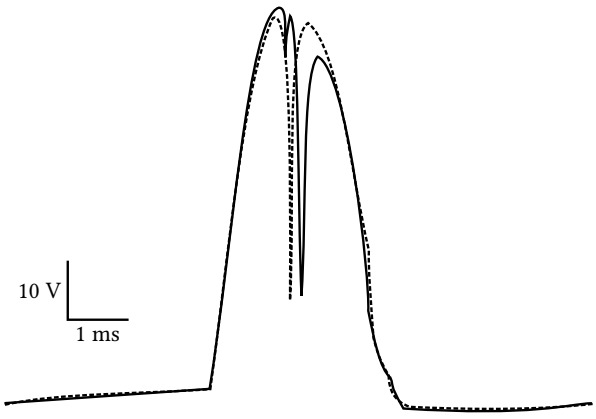

Figure 10. Oscilloscope view of a klystron mode (vectorized) with empty cavity (dashed) and with DPPH sample (stroked). The shift of the minimum due the modified resonator properties is clearly visible. The small dip in the stroked curve is the mark added by the reference resonator.

It is important to transform the whole recorded spectrum and not only a narrow range containing the peak as the peak wings covered by noised signal can carry significant information[2].

II.B Adjustment

First of all, we familiarized ourselves with the components of the setup[9]. The tunable devices were the klystron control unit, the EPR control unit, the modulation frequency generator, a resonator, the e-h-tuner and the lock-in amplifier. Additionally, the EPR control unit and the frequency generator could be connected to an digital oscilloscope. The teslameter and the EPR control unit both have been connected to a computer running *LabView* for data acquisition.

The *LabView* application itself took into account the measurement delay of the teslameter. Every time the EPR control unit performed another sweep, that is scanning through a user-defined range for the magnetic field strength B_0, both the data of the teslameter and of the lock-in amplifier have been recorded independently. Using the assumption that the EPR control unit scans the specified range linearly, the slight variations of the response of the teslameter have been flattened by performing a linear regression. As the output of the *LabView* application only contains the data after this recalibration, we can only work on this preprocessed output. Although the data is clearly not the original output of the experiment, we will refer to it as measured data in the following.

For calibration, we arbitrarily selected one klystron mode near 9.32 GHz. Using modes around 9.5 GHz is common[2, 3]; for pratical purposes, klystron modes of

Table II. Q factor and resonator frequencies. The data points *left half* and *right half* are used for the FWHM calculation. In order to compare them to the peak position, the average of these two is given as well. The shaded rows contain calculated values.

parameter		with DPPH	without DPPH
left half	[Mhz]	9322 ± 1	9330 ± 1
right half	[Mhz]	9326 ± 1	9334 ± 1
peak	[Mhz]	9324 ± 1	9331 ± 1
average	[Mhz]	9324 ± 2	9332 ± 2
FWHM	[Mhz]	4 ± 2	4 ± 2
Q		2300 ± 1600	2300 ± 1600

Table III. Peak quality q (see text) and SNR for different modulation amplitudes B_1 and the DPPH sample. As the data points are quite distinct, we did not calculate any errors estimations.

U_M [V]	B_1 [mT]	SNR	ΔI [a.u.]	ΔB [mT]	q [a.u.]
0.25	0.04	68	2.2	0.27	8.3
0.75	0.12	190	6.4	0.28	23
1	0.16	250	8.1	0.30	27
1.25	0.2	270	8.8	0.32	28
1.5	0.24	290	9.7	0.35	28
2	0.32	320	10	0.36	29
2.5	0.4	340	11	0.41	27
5	0.8	300	9.8	0.69	14
10	1.6	220	7.2	1.4	5.2

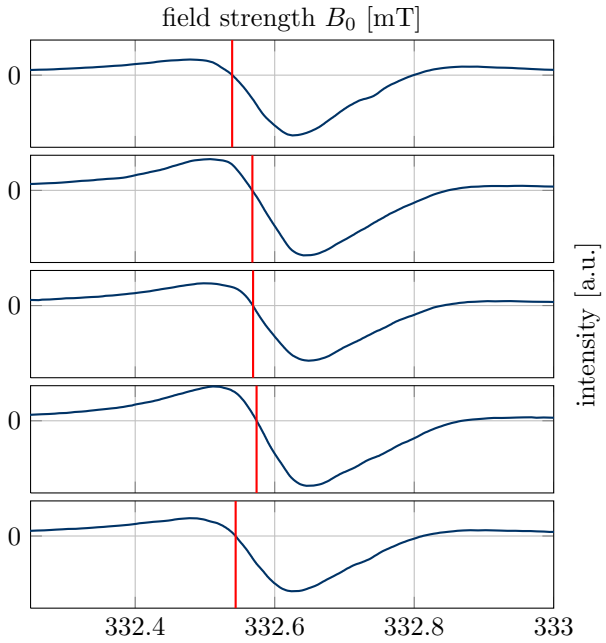

Figure 11. Various spectra of the DPPH sample recorded during the microwave phase adjustment. For neither of the settings, we were able to achieve a pointsymmetric curve. The thick vertical bars denote the zero crossing of the different peaks. As the microwave phase changes the shares of the measured signal referring to absorption and dispersion, the zero crossing differs as well. The relative intensities are to scale.

high intensity[3] and high spin sensitivity[10] are selected. As the frequency heavily influences the calculated g factors, it had to be measured precisely. This has been done by adjusting a resonator in the waveguide, which yielded small absorption peaks observable with the oscilloscope. An example is given in Figure 10. The same way, we determined the FWHM of the resonator dip on the klystron mode. An e-h-tuner between the klystron and the resonator cavity helped shaping the resonator peak. We used the two screws of the e-h-tuner to enhance the quality factor and aiming for a deep dip in the klystron mode.

We determined the resonator frequency and the Q factor for both with and without the DPPH sample as shown in Table II. The rather large error for the Q factor is due to the high relative error of the FWHM which in turn is caused by the mechanical clearance of the reference resonator that has been used to determine the frequencies. However, the Q factor matches the typical range for this setup[3, 10]. The small shift in the frequency for the DPPH sample is due to the quartz sample tube, because the quartz tube has dielectric properties different from the ones of air.

The e-h-tuner allows to shift the phase of the microwave signal. As the initial signal was asymmetric (cf. Figure 11), we tried to find an optimal pointsymmetric setting. The asymmetry is due to the competing effects of dispersion and absorption. In Figure 11, the shift of the peaks zero crossing due to the phase change is clearly visible.

Next, we optimized the lock-in modulation amplitude. The modulation frequency ω' itself was fixed and followed the specification of the manufacturer of the EPR control unit. ω' was fluctuating around 1 kHz. For the calculation of the g factors, the exact value of ω' is unimportant. The modulation amplitude was determined by the output voltage of the frequency generator, that could be measured with the oscilloscope. In principle, a simple voltmeter should do the job as well. As the exact value of the modulation voltage U_M or, more specifically, the modulation field strength B_1 is unimportant for the results as well, we used the oscilloscope only to estimate the voltage. The corresponding field strength can be calculated by[9]

$$B_1 = 0.16 \, \frac{\mathrm{mT}}{\mathrm{V}} U_M \tag{25}$$

In order to evaluate the quality q of the spectra, we looked at the peak to peak distance ΔI and compared it to the peak width. The latter has been defined as the distance ΔB between the zero crossings. This is justifiable, as the ratio of the positive peak height to the negative peak height is mostly constant as long as the peak shape itself

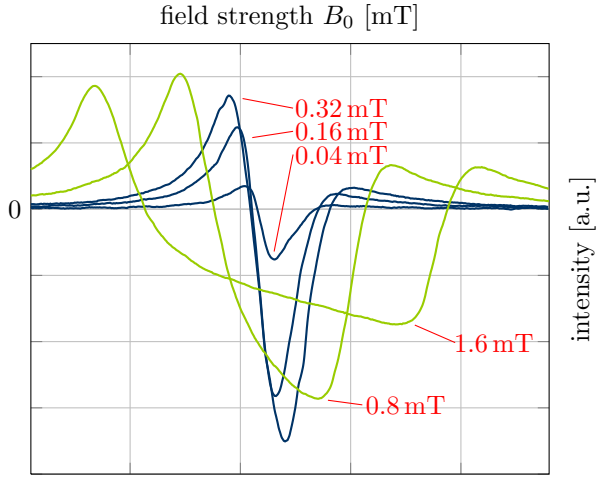

Figure 12. Peak shape depending on the modulation amplitude B_1 (red values in the diagram). For clarity, only five out of nine peaks are presented in this diagram. The properties of these shapes are listed in Table III.

is not distorted.

$$q := \frac{\Delta I}{\Delta B} \tag{26}$$

As the microwave phase settings were left untouched during this part of the adjustment, this criterion is suitable to compare the peaks. The signal to noise ratio (SNR) only optimizes for high peak to peak distances, as the the noise is of rather constant amplitude for all modulation amplitudes. Table III gives both the SNR and q. According to the SNR criterion, 2.5 V would be optimal. However, we sticked to the more sensitive q criterion and chose 2 V (corresponding to $B_1 = 0.32$ V) as optimal value. Figure 12 shows various peak shapes depending on the modulation amplitudes. For clarity, only some of the recorded shapes are presented in the diagram.

Figure 13 visualizes the data from Table III. With increasing modulation amplitude, the line width increases as well. For all other values of interest (peak to peak-distance, q and SNR), there is a maximum near to 2 V. For high modulation amplitudes, the peaks get distorted due to relaxation interaction of the spins with the modulation field B_1.

The lock-in phase was optimized with respect to maximum signal intensity. As the sign of the signal itself is of no physical importance, we neglected the sign at all. All the following spectra have been recorded with a lock-in phase of -6 degrees.

The SNR is heavily influenced by another setting: the microwave power of the klystron. Actually, the klystron output power is constant. A filter right before the e-h-tuner can be used in order to suppress radiation intensity. As we could inspect an unused attenuator, we could compare the construction type to reference sketches[1]. It is found to be a linear vane attenuator of dated

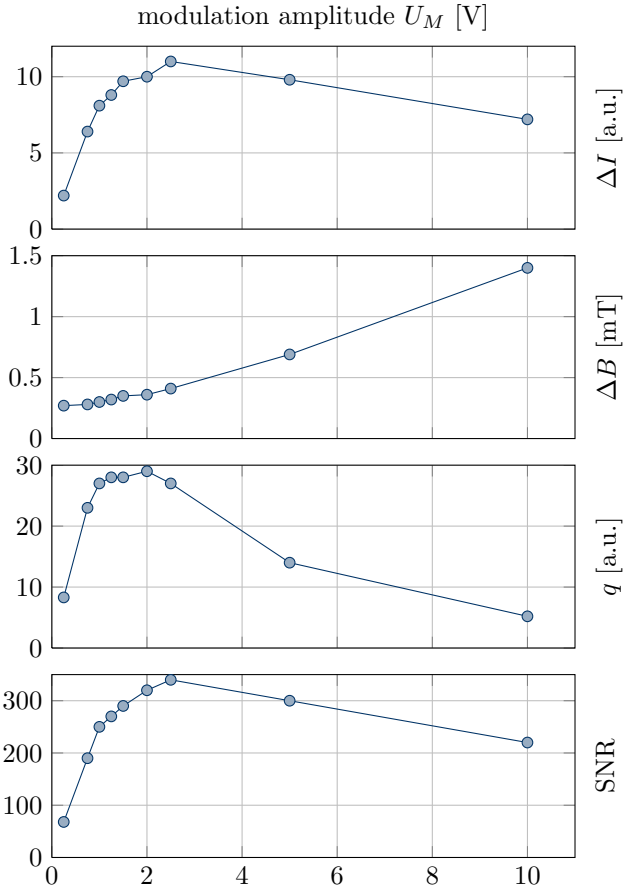

Figure 13. Dependency of the peak to peak-distance ΔI, the line width ΔB, the q factor (see text), and the SNR on the modulation amplitude as listed in Table III.

Table IV. Peak quality q (see text) and SNR for different microwave power settings α and the DPPH sample. β denotes the scaling factor of the spectra and, hence, the relative intensity. Three values could not be determined (see text and Figure 14).

α [a.u.]	β	SNR	ΔI [a.u.]	ΔB [mT]	q [a.u.]
5.2	0.19	88	2.9	0.36	8.0
5.4	0.42	190	6.3	0.38	17
5.6	1.0	460	15	0.37	40
5.65	1.3	570	19	0.39	49
5.7	1.6	710	24	0.37	15
6	6.5	–	–	0.36	–

construction[3]. For this type, the dependency of the attenuation on the adjustment knob is highly non-linear[1]. Hence, we can only record SNR and intensity with respect to the micrometer adjustment α. Table IV gives the SNR and the signal intensity for all measurements. Excluding the peaks which show saturation effects, the curves can be transformed into one another by multiplication with a scaling factor β. This factor is given in Table IV as well.

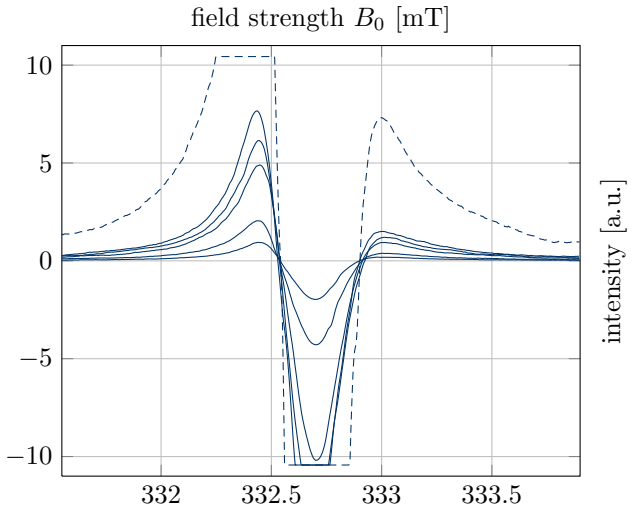

Figure 14. DPPH spectra for different microwave intensities. See Table IV. The properties of the dashed dataset could not be determined precisely.

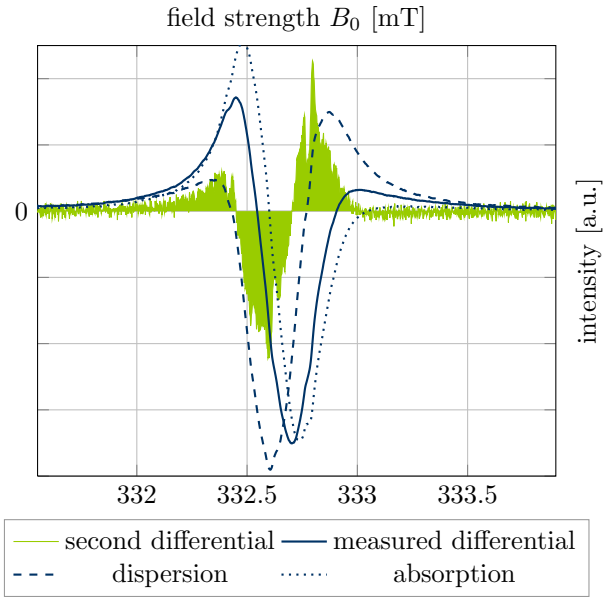

Figure 15. Measured differential spectrum (stroked) together with its decomposition parts for dispersion (dashed) and absorption (dotted). In order to amplify the visibility of the peak structure, the second derivative has been calculated (filled). For the interpretation, see text.

As we cannot determine an absolute intensity, relative intensities will be expressed in terms of β. The peak without saturation effects that is of the highest intensity defines $\beta = 1$. Values exceeding 1 therefore denote saturated peaks. The corresponding β values are prone to errors as only a partial peak shape can be used in order to determine β. Scaling one curve with the corresponding β reproduces the reference peak shape for all measured spectra very well. This supports the assumption, that the attenuator has no effect on the physical results of the spectra besides amplification. For saturated peaks, there is a clearly visible shift towards lower field strengths B_0.

Over the range of α we looked at, $\beta(\alpha)$ was a exponential function. In physical terms, the intensity scaled exponentially with increasing adjustment values α. Linear regression on the logarithm of β gave a coefficient of determination of 0.998. As this is of minor physical interest, we refrained from further investigation.

All spectra for various microwave intensities are given in Figure 14.

II.C DPPH

After the setup adjustment, we could start to actually measure sample properties. As DPPH was used for the setup evaluation, we can use the recorded data from the previous section. As Figure 15 shows, the measured signal is very clear. The Hilbert transformation recognizes the spectrum to be dominated by dispersion and detects the dispersion peak to be at 332.605 mT, whereas the absorption zero crossing is at 332.601 mT. Averaging yields resonance at (332.603±0.003) mT. This very small relative error of about 10^{-5} however, is completely obliterated by the relative error of the reference frequency as given in Table II.

Although the spectrum in Figure 15 clearly shows significant dips, which could be amplified by calculating the second differential spectrum, the resolution is too low to resolve the peaks. We assume these peaks to be the hyperfine structure of DPPH. For solutions, the hyperfine structure is rather coarse with linewidths of 0.5 mT[15] but gets very narrow (0.01 mT) for solids[3]. The variation of the linewidths inbetween is smooth and continuous[16], hence we can justify this explanation of the dips in our spectra, as the dips have a width of some 0.04 mT.

Together with the information in Table II, the g factor can be calculated from equation 11 with an error according to Gaussian error propagation of

$$\Delta g = g\sqrt{(\delta B_0)^2 + (\delta\omega)^2} \tag{27}$$

where δx is the relative error of parameter x.

$$g = (2,0029 \pm 0,0003)$$

This is compatible with the reference value given in Table I with a relative error of about 10^{-4}.

II.D Tempol

For tempol, we adjusted the setup again in order to get a signal with high intensity. Figure 16 shows the best spectrum out of the thirteen spectra we measured together with its decomposition. We found three peaks. The resulting peak positions are presented in Table V. The peaks are mostly of the same intensity, only the rightmost one is a bit smaller than the other two. The middle peak, corresponding to $m_I = 0$, could be used for

Table V. Results for the tempol sample after decomposition. Peak positions, their shifted position after linear regression (see text) together with all g factors. The error of all g values is 0.0001, as the influence of correcting the positions on the error estimates is neglectable. For all peak positions, the error is 0.0065 mT.

	$m_i = -1$	$m_i = 0$	$m_i = 1$
dispersion peak [mT]	330.729	332.335	333.943
absorption zero crossing [mT]	330.716	332.323	333.930
average [mT]	330.723	332.329	333.937
corrected position [mT]	332.3295	–	332.3295
g factor	2.0046	2.0046	2.0046

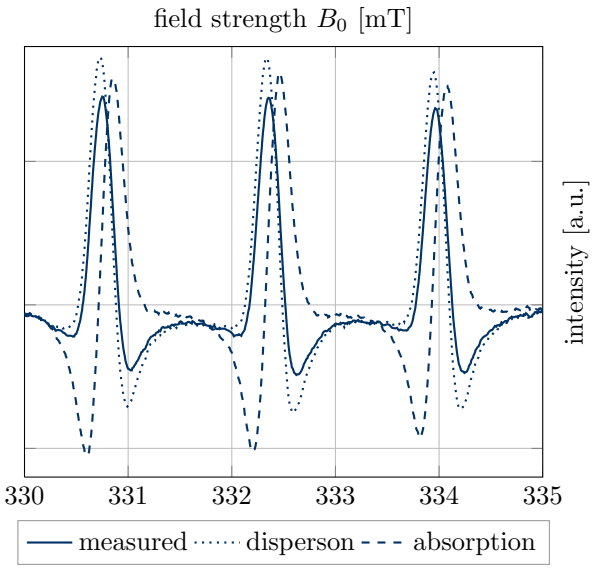

Figure 16. Measured spectrum of tempol with its decomposed parts of absorption and dispersion.

calculation of the g factor directly. The other two are equally shifted away from the middle as their energy level is given by

$$E = E_0 + am_I \tag{28}$$

where E_0 is the energy of the $m_I = 0$ level and a is an isotropic splitting constant. The anisotropic part is averaged out in the solution. Using linear regression, we could determine $a = (1.607 \pm 0.006)$ and hence, calculate the g factor for the peaks with $m_I \neq 0$. All g factors are given in Table V. The average isotropic g factor is

$$g = (2.0046 \pm 0.0002)$$

This value is only slightly below the reference value in Table I and clearly compatible with it.

As a regression line based on three points and a coefficient of determination with seven significant nines is rather unsurprising and unhelpful, we omitted the diagram.

II.E Vanadyl

We investigated the vanadyl spectrum the same way we did for tempol. After adjustment, we had seven spectra to choose from. Figure 17 presents the visualization and Table VI lists the corresponding peak data. As expected, we got eight peaks due to the hyperfine splitting. This time, we get $a = (10.64 \pm 0.04)$ from linear regression with a coefficient of determination of 0.9988. This is pretty much a straight line with dots on it, hence we omitted plotting the regression line, again.

The intensities for the vanadyl sample are kind of symmetric—but have a center of symmetry left of $m_I = 0$, which is not expected, as in the spectrum there are more peaks to the right of the center of symmetry for the intensities. Even more interesting is the substructure of the eight peaks. As shown in Figure 17, most of the peaks seem to consist of two separate peaks.

The average value of the g factors in Table VI give the isotropic g factor for vanadyl

$$g = (1.9711 \pm 0.0003)$$

which is identical to the reference value from Table I.

II.F Copper sulfate

After a new adjustment round, the selected klystron mode has changed. The central peak position was determined as before as measured to be (9325 ± 2) MHz.

For this material, we had two samples to choose from: polycrystalline powder and a single crystal. For the first sample, we will only present a rough qualitative analysis, whereas the properties of the second sample will be investigated in detail.

The raw spectra recorded for the polycrystalline powder are rather irregular. Again, we calculated the decomposition into absorption and dispersion. The absorption spectrum has been integrated, as this is the suggested way of analyzing powder spectra[6]. For the range between the two peaks in the integral spectrum, there is an approximation[6]

$$I(g) = \frac{C}{\sqrt{g_\perp - g}} \tag{29}$$

where C is a constant mostly influenced by the behavior of the setup. This function uses g as parameter in order to simplify the equation. Of course, the g factor has to be converted to a magnetic field strength B_0. The crossing of the integral spectrum with this function scaled by a factor of 0.5 is supposed[6] to be an estimate for $g_\parallel$. Figure 18 presents both the spectra and the fitting lines. As this is an uncontrolled approximation, we only present the resulting values for this method.

$$g_\parallel = 2.06 \qquad g_\perp = 2.24$$

Even though this method seems to be less accurate than the method for the single crystal, the results are compatible with the reference data presented in Table I.

Table VI. Results for the vanadyl sample after decomposition. Peak positions, their shifted position after linear regression (see text) together with all g factors. The error of all g values is 0.0001, as the influence of correcting the positions on the error estimates is neglectable. For all peak positions, the error is 0.012 mT, that is the average error introduced by different results for the dispersion peak and the absorption zero crossing. The corrected positions match $m_I = 0$.

	$m_i = -7/2$	$m_i = -5/2$	$m_i = -3/2$	$m_i = -1/2$	$m_i = 1/2$	$m_i = 3/2$	$m_i = 5/2$	$m_i = 7/2$
dispersion peak [mT]	301.888	311.574	321.574	331.78	342.35	353.148	364.7	376.638
absorption zero crossing [mT]	301.91	311.654	321.544	331.78	342.349	353.262	364.746	376.601
average [mT]	301.899	311.614	321.559	331.780	342.350	353.205	364.723	376.620
corrected position [mT]	339.153	338.224	337.525	337.102	337.0275	337.239	338.113	339.3655
g factor	1.9642	1.9696	1.9737	1.9762	1.9766	1.9754	1.9703	1.9630

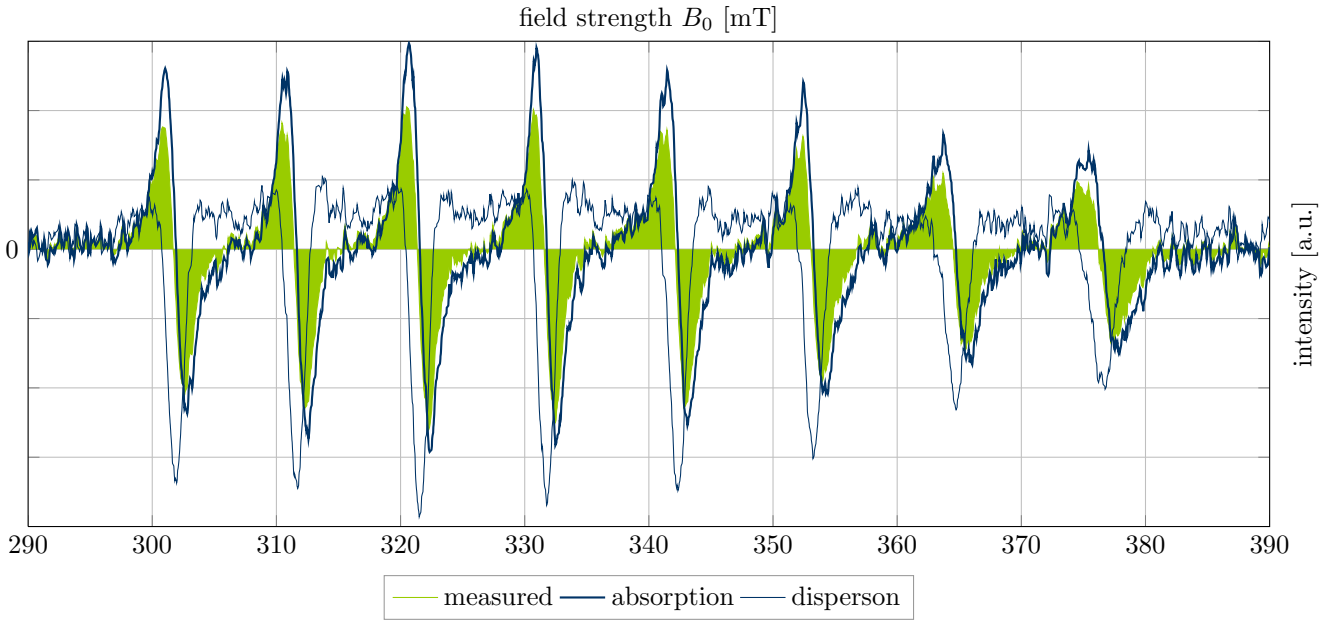

Figure 17. Measured spectrum of vanadyl (filled) with its decomposed parts of absorption (thick line) and dispersion (thin line). This time, the decomposition is very good as the absorption extrema are of nearly equal height for both positive and negative peaks.

For the solid crystal, we recorded 36 spectra with a rotational difference of 10 degrees after doing four spectra for adjustment. For each spectrum, we computed the decomposition. The dispersion parts gave the best results. As the rotation angle of the crystal relative to the scale given on the sample holder is not known, we had to determine the offset at first. By coincidence, the offset is very close to zero. We split the peak positions according to the quadrants they belong to. The positional error has been estimate the same way as before: the difference between the absorption zero crossing and the dispersion peak position. Table VII and Table VIII hold the data. In Figure 19, we plotted the four quadrants independently over $\sin^2\theta$, as the general dependency of g is given[1] by

$$g(\theta) = g_\parallel + (g_\perp - g_\parallel)\sin^2\theta \tag{30}$$

This way, we could use linear regression instead of non-linear fitting algorithms which are neither guaranteed to find the minimum nor do have to converge. We did not convert any of the peak positions to g factors in this step in order to diminish the influence of the g conversion error introduced by the rather large frequency error.

There are several interesting observations. All four regression lines share quite the same slope, that is give the same difference between $g_\perp$ and $g_\parallel$. Despite this similarity, the four lines form two groups: the ones recorded for the raising part of the sine and the ones recorded for the falling part. The former have a zero axis crossing higher than the one for the latter group. Although this looks like hysteresis, we can safely rule out this effect as there is no physical justification. It is more likely that the requirement, a proper alignment of the crystal with respect to the magnetic axis of the field B_0, is not met. This way, equation 30 does not hold anymore. In order to compensate for this effect, we will use the first group in order to determine the maximum of the sine which gives $g_\perp$ and the second group in order to determine the minimum for $g_\parallel$.

Table VII. Peak positions in mT for the single crystal of copper sulfate. These quadrants are those for the raising part of the sine (see text).

	quadrant A	quadrant C
10 degrees	304.479 ± 0.07	305.442 ± 0.30
20 degrees	308.233 ± 0.16	311.828 ± 0.32
30 degrees	308.747 ± 0.39	303.337 ± 0.29
40 degrees	311.309 ± 0.42	312.208 ± 0.34
50 degrees	314.909 ± 0.14	314.119 ± 0.31
60 degrees	315.956 ± 0.12	315.952 ± 0.34
70 degrees	316.216 ± 0.08	317.886 ± 0.24
80 degrees	317.322 ± 0.06	318.282 ± 0.02
90 degrees	319.264 ± 0.12	316.288 ± 0.02
R^2	0.95	0.89
slope	0.18	0.19
axis crossing	304.1	304.9

Table VIII. Peak positions in mT for the single crystal of copper sulfate. These quadrants are those for the falling part of the sine (see text).

	quadrant B	quadrant D
10 degrees	$303.725, \pm 0.25$	$304.181, \pm 0.04$
20 degrees	$304.112, \pm 0.28$	$302.848, \pm 0.13$
30 degrees	$303.083, \pm 0.12$	$306.071, \pm 0.09$
40 degrees	$304.085, \pm 0.01$	$304.558, \pm 0.13$
50 degrees	$308.267, \pm 0.01$	$306.864, \pm 0.29$
60 degrees	$309.223, \pm 0.11$	$309.027, \pm 0.28$
70 degrees	$313.928, \pm 0.17$	$312.281, \pm 0.22$
80 degrees	$316.253, \pm 0.16$	$314.451, \pm 0.18$
90 degrees	$316.868, \pm 0.17$	$317.445, \pm 0.11$
R^2	0.89	0.68
slope	0.17	0.16
axis crossing	299.9	299.1

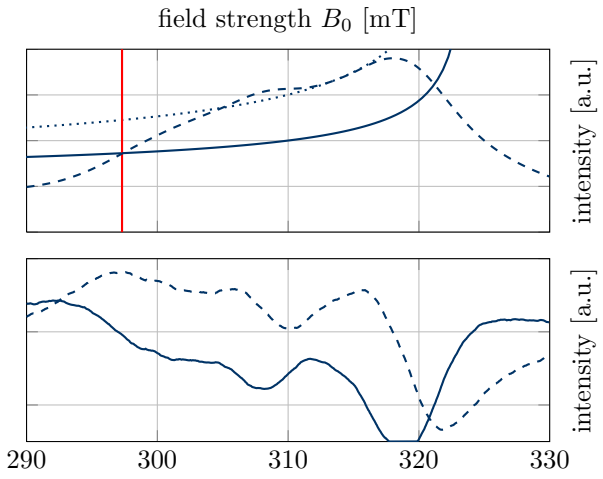

Figure 18. Integral (top) and differential (bottom) spectrum for the polycrystalline copper sulfate sample. The fitting curves (stroked and dotted) are determined manually (see text). The red bar in the upper spectrum denotes the crossing (see text). The differential spectrum contains both components, absorption (dashed) and dispersion (stroked).

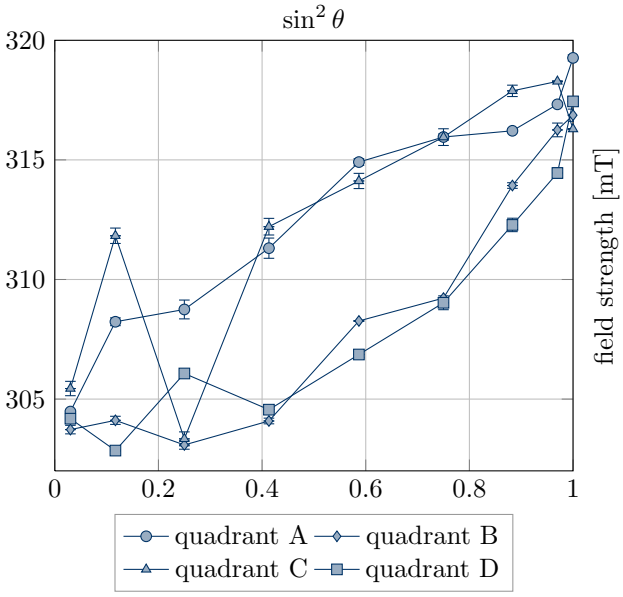

Figure 19. Measured peak positions of the single crystal copper sulfate for all four quadrants (see text). For clarity, the regression lines are not included.

Using the data in Table VII, we get

$$g_\perp = (2.092 \pm 0.003)$$

and from the data in Table VIII, we can calculate

$$g_\parallel = (2.211 \pm 0.003)$$

The errors have been calculated from the weighted averages of the results for the two regression lines from each group. The first value is identical to the reference one, but the second one differs significantly from the data in Table I. We attribute this error to the systematic misalignment of the crystal.

III Discussion

We recorded spectra for DPPH, tempol, vanadyl, and copper sulfate (both polycrystalline and single crystal). All spectra showed the expected features, although the DPPH hyperfine splitting was not measureable.

During the adjustment, we could clearly see the dependency of the signal quality on the modulation amplitude and the microwave power.

All spectra have been analyzed using the Kramers-Kronig relations, which lead to very small relative errors. The resonance positions could be reproduced in all cases with one exception: $g_\parallel$ for the single crystal does not match the reference value. We attribute this deviation

to a tilted position of the crystal structure. All other g factors are at least compatible with the reference ones; the g value for vanadyl and the $g_\perp$ for the single crystal of copper sulfate is identical to the reference one.

[1] C. P. Poole, *Electron Spin Resonance: A comprehensive treatise on experimental techniques* (Interscience Publishers, 1967).

[2] M. Bersohn and J. C. Baird, *An introduction to electron paramagnetic resonance* (W A Benjamin, 1966).

[3] S. K. Misra, *Multifrequency Electron Paramagnetic Resonance* (Wiley-VCH, 2011).

[4] A. Carrington, *Introduction to Magnetic Resonance* (Harper and Row, 1969).

[5] W. Demtröder, *Experimentalphysik 3* (Springer, 2010).

[6] L. A. Bljumenfeld, W. W. Wojewodski, and A. G. Semjonow, *Die Anwendung der paramagnetischen Elektronenresonanz in der Chemie* (Akademische Verlagsgesellschaft, 1966).

[7] Chemspider, http://www.chemspider.com/ChemicalStructure.2016757.html (2013).

[8] E. Shuter, S. J. Rettig, and C. Orvig, Acta Crystallographica Section C **51**, 12 (1995).

[9] *Lab Course Introduction on Electron Paramagnetic Resonance* (FU Berlin, 2013).

[10] J. R. Pilbrow, *Transition Ion Electron Paramagnetic Resonance* (Clarendon Press, 1990).

[11] G. Jeschke, *"Einführung in die ESR-Spektroskopie"* (1998).

[12] Chemspider, http://www.chemspider.com/ChemicalStructure.121639.html (2013).

[13] W. V. Smith, P. P. Sorokin, I. L. Gelles, and G. J. Lasher, Phys. Rev. **115**, 1546 (1959).

[14] R. M. Deal and W. S. Koski, The Journal of Chemical Physics **31**, 1138 (1959).

[15] N. W. Lord and S. M. Blinder, The Journal of Chemical Physics **34**, 1693 (1961).

[16] S. Kolaczkowski, J. Cardin, and D. Budil, Applied Magnetic Resonance **16**, 293 (1999).

[17] M. Peter, D. Shaltiel, J. H. Wernick, H. J. Williams, J. B. Mock, and R. C. Sherwood, Phys. Rev. **126**, 1395 (1962).